

# Point Defects in a Two-Dimensional ZnSnN<sub>2</sub> Nanosheet: A First-Principles Study on the Electronic and Magnetic Properties

Asadollah Bafekry,\* Mehrdad Faraji, Mohamed M. Fadlallah, Bohayra Mortazavi, A. Abdolhazadeh Ziabari, A. Bagheri Khatibani, Chuong V. Nguyen, Mitra Ghergherehchi,\* and Daniela Gogova

Cite This: *J. Phys. Chem. C* 2021, 125, 13067–13075

Read Online

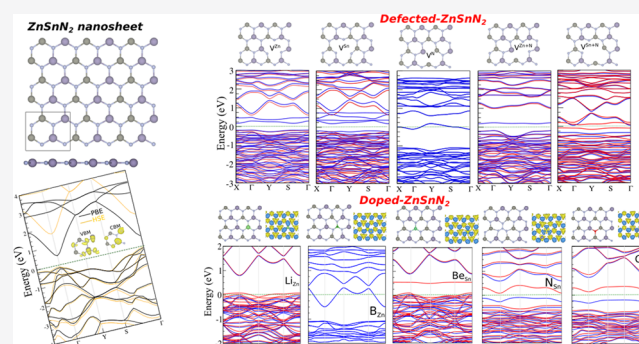
ACCESS |

Metrics & More

Article Recommendations

Supporting Information

**ABSTRACT:** The reduction of dimensionality is a very effective way to achieve appealing properties in two-dimensional materials (2DMs). First-principles calculations can greatly facilitate the prediction of 2DM properties and find possible approaches to enhance their performance. We employed first-principles calculations to gain insight into the impact of different types of point defects (vacancies and substitutional dopants) on the electronic and magnetic properties of a ZnSnN<sub>2</sub> (ZSN) monolayer. We show that Zn, Sn, and N + Zn vacancy-defected structures are p-type conducting, while the defected ZSN with a N vacancy is n-type conducting. For substitutional dopants, we found that all doped structures are thermally and energetically stable. The most stable structure is found to be B-doping at the Zn site. The highest work function value (5.0 eV) has been obtained for Be substitution at the Sn site. Li-doping (at the Zn site) and Be-doping (at the Sn site) are p-type conducting, while B-doping (at the Zn site) is n-type conducting. We found that the considered ZSN monolayer-based structures with point defects are magnetic, except those with the N vacancy defects and Be-doped structures. The ab initio molecular dynamics simulations confirm that all substitutionally doped and defected structures are thermally stable. Thus, our results highlight the possibility of tuning the magnetism in ZnSnN<sub>2</sub> monolayers through defect engineering.



## INTRODUCTION

Group II–IV nitrides, as a collection of ternary heterovalent compounds, are composed of earth-abundant elements. The II–IV nitrides are very similar to the III-nitrides (III = Al, Ga, and In) and are made of each group III element with periodically varied group II and IV elements. Although group III-nitrides have been extensively studied, the II–IV nitrides have not attracted enough attention so far. However, potential applications of these materials are conceivable.<sup>1</sup> Among the II–IV nitrides, the Zn–IV–N<sub>2</sub> class has attracted more attention.<sup>2</sup> The advantages of Zn–IV–nitrides relative to the nitrides of group III are as follows: (i) abundant natural elements as constituents, making them cost-effective; (ii) absence of phase separation across the whole alloying range; (iii) environmental friendliness;<sup>2</sup> and (iv) facility for p-type doping and controlling by an easy combination of elements and retrieving the defects.<sup>3,4</sup> Unlike the materials with ionic and covalent bonding, the median bonding nature of Zn–IV–N<sub>2</sub> makes them more practical.<sup>4</sup> ZnSnN<sub>2</sub> as an inseparable member of the class of Zn–IV–nitrides can be used in different fields such as photovoltaics, optoelectronics, photocatalysis, etc.<sup>2–8</sup> It also presents spontaneous polarization and piezoelectric effects.<sup>9</sup> Furthermore, a large absorption coefficient in the

range of UV–Vis–NIR is attributed to the ZnSnN<sub>2</sub> material, which makes it competitive with more commonly used photovoltaic materials such as GaAs, CdTe, and InP.<sup>2,7,10</sup> ZnSnN<sub>2</sub> can fulfill the tetrawatt power requirement with its very low cost and environmental compatibility<sup>7</sup> by plentiful and nontoxic materials.<sup>11</sup> Due to these favorable properties, ZnSnN<sub>2</sub> is appealing in terms of both economic and environmental aspects.<sup>12</sup>

Despite all of these attractive properties, ZnSnN<sub>2</sub> is still at the beginning of its development and investigation.<sup>5</sup> It is a rather undeveloped member of the Zn–IV–N<sub>2</sub> family and the knowledge about ZnSnN<sub>2</sub> is scarce and somewhat contradictory.<sup>2,10,13</sup> The first computational research was reported in 2008.<sup>14</sup> The ZnSnN<sub>2</sub> thin film was first synthesized in 2012,<sup>15,16</sup> and its powder form was first prepared in 2016.<sup>11,17</sup> Recently, the first single-crystalline ZnSnN<sub>2</sub> material has been reported.<sup>2</sup> For

Received: April 26, 2021

Revised: May 18, 2021

Published: June 3, 2021



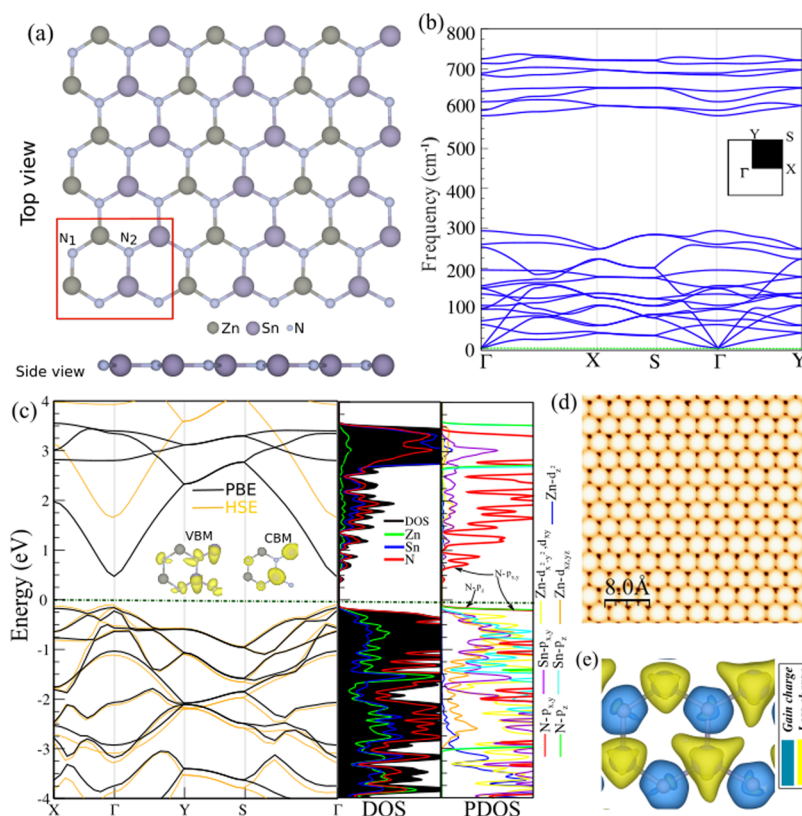


**Figure 1.** (a) Top and side views of the atomic structure, (b) phonon dispersion, (c) electronic band structure (within PBE and HSE06) with corresponding DOS and projected DOS (PDOS), (d) simulated STM profile, and (e) charge density difference of the ZSN monolayer. The primitive unit cell used in calculations is shown by the red rectangle. Zero of energy is set to the Fermi level.

this purpose, many investigations have been started to elucidate the electronic, optical, and other properties of  $\text{ZnSnN}_2$ .<sup>10,18,19</sup> Based on the cation-sublattice ordering, two phases of  $\text{ZnSnN}_2$  are available (i.e., ordered and disordered phases). The ordered phase is made by a periodic substitution of the Zn and Sn inside the wurtzite symmetry, which eventually results in an orthorhombic structure. In the disordered phase cation sublattice, Zn and Sn are placed randomly in the wurtzite-like structure.<sup>10,18</sup>

Strictly speaking, for  $\text{ZnSnN}_2$ , three major factors should be considered: (i) Point-defect properties. Any point defect should be fully distinguished since they affect electrons and/or hole recombination causing loss of photovoltaic cell efficiency.<sup>20</sup> (ii) The discrepancy between theoretical and experimental values of the band gap.<sup>19</sup> The calculated band gap values are in the range of 0.35–2.64 eV according to the calculation method and the hypothetical crystal symmetry.<sup>21,22</sup> Based on first-principles calculations, a value of about 2 eV is obtained for the band gap.<sup>12</sup> However, the Heyd–Scuseria–Ernzerhof (HSE) hybrid functional calculations result in band gap values of 1.42 and 1.84 eV.<sup>23,24</sup> A band gap value of 2 eV was determined based on the PBE0 hybrid functional calculations.<sup>15</sup> According to the local-density approximation (LDA), lattice parameters were obtained in the study by Punya and co-workers, and a gap of 2.15 eV was calculated using the quasiparticle self-consistent GW method. Using experimental values of the lattice parameters, they reported a band gap value of 1.8 eV.<sup>25</sup> Utilizing the special quasi-random structure (SQS), it was shown that the band gap value reduces from 2.1 to 1.1 eV by altering the cation ordering from maximum to minimum order. The calculation was performed based on hybrid density functional theory (DFT).<sup>6</sup>

According to experimental results, which rely on the absorption or photoluminescence spectra, a wider range of band gap values were reported, e.g., from 0.95 to 2.38 eV.<sup>12,26,27</sup> This obvious discrepancy between the theoretical and experimental values is justified by different reasons such as band filling due to degenerate carrier density and alteration in cation ordering/disordering leading to the fundamental band gap changes.<sup>13</sup> (iii) Undesirable n-type doping. The electron carrier concentration adversely increases to  $1021 \text{ cm}^{-3}$ ,<sup>13</sup> which is in the range of the metallic structures according to the Hall measurements.<sup>28</sup> The source of such a high concentration of electrons is not clear; however, the coexistence of elemental metal phases or the formation of intrinsic defects may be influential.<sup>28</sup> Such high concentrations lead to a meaningful Burstein–Moss shift, which may be responsible for the larger band gap values. The formation of donor-type point defects may also be related to the Burstein–Moss shift.<sup>5,20</sup> Apart from the electron carrier concentration, the low mobility values are also a drawback that limit its device application.<sup>29,30</sup> Until now, various aspects of the Zn–IV–N<sub>2</sub> semiconductors have been considered, such as crystal structure, thin-film growth, cation ordering, phonons, elasticity and piezoelectric properties, electronic band structure, energies of formation, and electrical conductivity,<sup>2,31</sup> but apparently native point defects, interstitials, and doping effects are relatively unexplored. As we know, two-dimensional (2D) materials possess wonderful electro-optical and optoelectrical properties compared to their three-dimensional (3D) counterparts.<sup>32</sup> Especially in photocatalysis, the 2D material not only has a high specific surface but also reduces the migration distance of the photogenerated electrons and holes; hence, the possibility of electron–hole recombination is minimized. Computational

**Table 1. Structural and Electronic Parameters Including the Lattice Constants  $a$ ,  $b$ , Zn–N ( $d_{\text{Zn-N}}$ ) and Sn–N ( $d_{\text{Sn-N}}$ ) Bond Lengths, Cohesive Energy Per Atom ( $E_{\text{coh}}$ ), Charge Transfer ( $\Delta Q$ ) between Atoms, Work Function ( $\Phi$ ), and Band Gap ( $E_{\text{g}}$ ) of PBE and HSE06 Are Shown Outside and Inside Parentheses, Respectively**

	$a$ ( $b$ ) (Å)	$d_{\text{Zn-N}}$ (Å)	$d_{\text{Sn-N}}$ (Å)	$q$ (e)	$E_{\text{coh}}$ (eV)	$\Phi$ (eV)	$E_{\text{g}}$ (eV)
ZSN	6.82 (5.91)	1.92	1.96	−1.3	−27.5	4.62	0.64 (1.71)

investigations can accelerate the design of 2D materials. The reduction of dimensions may be an effective path to gain novel properties for layered or nonlayered materials.<sup>8</sup> Different aspects of 2D materials can be investigated, such as point defects (vacancies, substitutional doping, antisites), adsorbing atoms, and grain boundaries along with mechanical, thermal, electronic, and optical properties.<sup>33,34</sup>

In this study, we have modified and simulated the 2D ZnSnN<sub>2</sub> (ZSN) structure using an ab initio method. Different kinds of vacancies such as single Zn ( $V^{\text{Zn}}$ ), Sn ( $V^{\text{Sn}}$ ), and N ( $V^{\text{N}}$ ) vacancies and double N + Zn and N + Sn vacancies are considered in detail. Furthermore, a number of substitutional dopants are used to modify the electronic structure of the 2D ZSN monolayer. The Zn atom is replaced by Li ( $\text{Li}_{\text{Zn}}$ -ZSN) and B ( $\text{B}_{\text{Zn}}$ -ZSN). The Sn atom is substituted by Be ( $\text{Be}_{\text{Sn}}$ -ZSN) and by N ( $\text{N}_{\text{Sn}}$ -ZSN). For an anionic dopant, the N atom is replaced by an oxygen atom ( $\text{O}_{\text{N}}$ -ZSN). The role of impurities and dopants is exceptionally significant in the 2D materials since they not only ensure a means for tuning the carrier concentration but also have implications for the interface properties of future 2D device heterostructures.

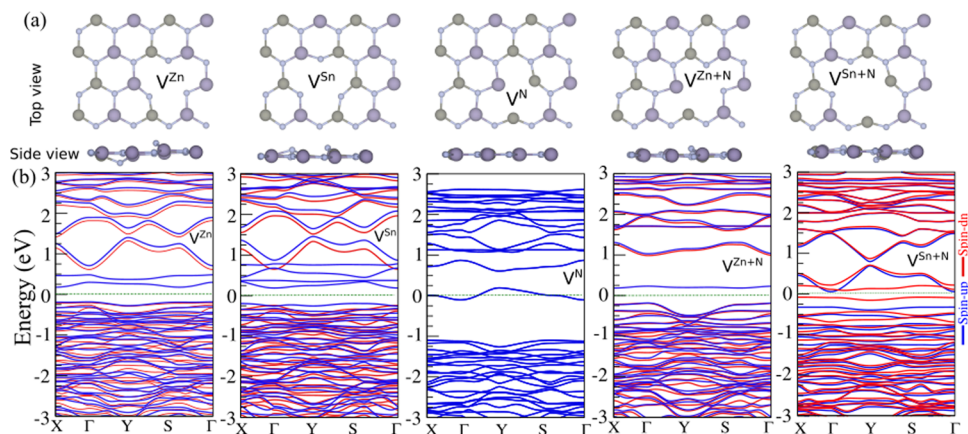
## METHODS

First-principles calculations were performed using the plane-wave basis projector augmented wave (PAW) method employed in the framework of density functional theory (DFT). The generalized gradient approximation (GGA) in the form of the Perdew–Burke–Ernzerhof (PBE)<sup>35,36</sup> functional was taken into account for the exchange–correlation potential as implemented in the Vienna Ab initio Simulation Package (VASP).<sup>37,38</sup> The kinetic energy cutoff of 600 eV was used for the plane waves. The Brillouin zone sampling was carried out using a  $\Gamma$ -centered  $16 \times 16 \times 1$   $k$ -point mesh for the primitive cell. The geometries were optimized until the energy difference between the following two steps was less than  $10^{-5}$  eV and the maximum force on atoms was smaller than  $10^{-3}$  eV Å<sup>−1</sup>. Moreover, for band structure calculations, the Heyd–Scuseria–Ernzerhof (HSE06)<sup>39,40</sup> screened-nonlocal-exchange functional of the generalized Kohn–Sham scheme was employed for more accurate band gap calculations. The van der Waals correction proposed using the DFT-D2 method of Grimme was implemented to describe the long-range vdW interactions.<sup>42</sup> The electronic charge transfers were calculated with a decomposition of charge density into atomic contributions by applying the Bader charge analysis technique.<sup>41</sup> The dynamical stability was examined in terms of the phonon band dispersions calculated by the small-displacement method using the PHONOPY code.<sup>43</sup> Simulated scanning tunneling microscopy (STM) images were obtained employing the Tersoff–Hamann theory.<sup>44</sup> STM-simulated images were graphed by means of WSxM software.<sup>45</sup> Ab initio molecular dynamics (AIMD) simulations have also been carried out to examine the thermal stability of the stability of defected and doped single-layer structures at 500 K and at room temperature (300 K) with a total simulation time of 6 ps and 2 fs time steps.

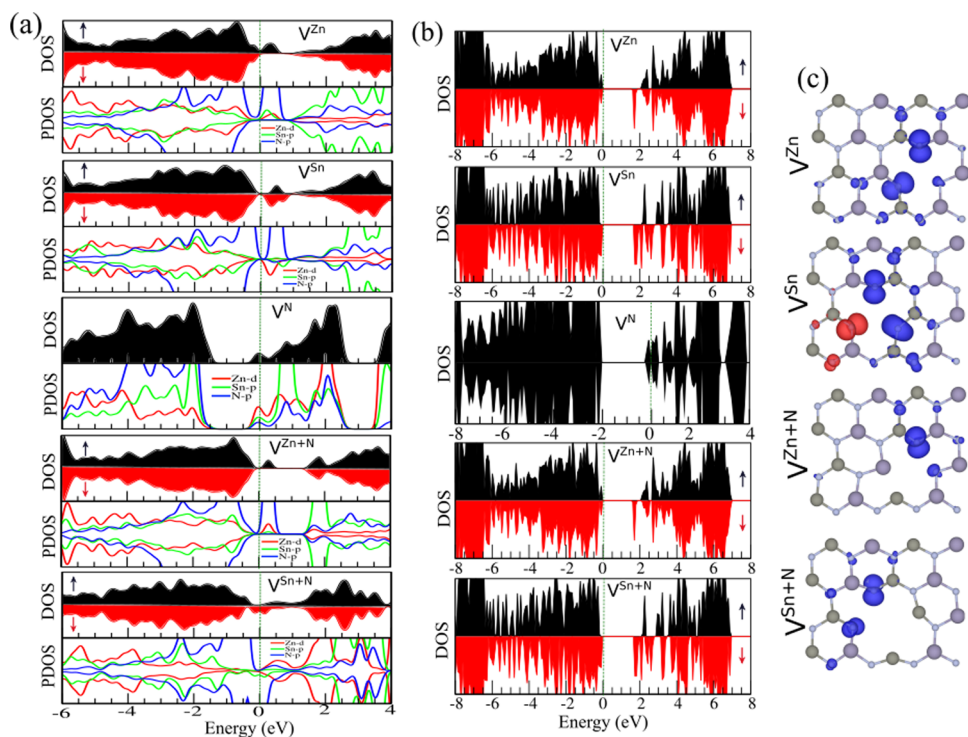
## RESULTS AND DISCUSSION

Figure 1a–e shows the top and side views of the atomic structure of the ZnSnN<sub>2</sub> monolayer, the calculated phonon dispersion curves, the calculated electronic band structure along with the total and projected density of states (DOS), the simulated STM profile, and the density of gain and loss charges, respectively. In the atomic structure of the ZSN monolayer, which has a rectangular primitive unit cell formed by two Zn, two Sn, and four N atoms, the lattice constants  $a$  and  $b$  are not equal vectors that make a 90° and it exhibits the  $P_{6m1}$  space group, as shown in Figure 1a. The optimized lattice constants are 6.82 and 5.91 Å, respectively, while the bond lengths of Zn–N and Sn–N are 1.92 and 1.96 Å, respectively. The optimized lattice constant and bond lengths are in good agreement with previous results.<sup>46</sup> The dynamical stability of the ZSN is verified by calculating its phonon band dispersion, which is depicted in Figure 1b. The monolayer of ZSN is found to possess dynamical stability in its free-standing form as examined by the phonon band dispersions through the whole BZ. Obviously, in the phonon branches, no imaginary frequencies are observed, which confirms the structure's dynamical stability. Apparently, all of the acoustical and optical phonon branches are free from any imaginary frequencies. There is a huge phonon gap between optical phonon branches probably arising from the different bonding characteristics of Zn–N/Sn–N and Zn–Sn atoms. It is known that the Zn–N and Sn–N bond stretching occurs at higher frequencies due to their strong bonding character. The structural parameters of ZSN are listed in Table 1. The difference in charge density ( $\Delta\rho$ ) is calculated using  $\Delta\rho = \rho_{\text{tot}} - \rho_{\text{Zn}} - \rho_{\text{Sn}} - \rho_{\text{N}}$ , where  $\rho_{\text{tot}}$ ,  $\rho_{\text{Zn}}$ ,  $\rho_{\text{Sn}}$ , and  $\rho_{\text{N}}$  represent the charge densities of the ZSN and of the isolated atoms, respectively (see Figure 1e). The Zn atom is positively charged, and the Sn atom is surrounded by negatively charged N atoms. Based on the charge transfer analysis, we found that the two types of N atoms in the atomic lattice of the ZSN gain 0.92e ( $N_1$ ) and 1.31e ( $N_2$ ) from the adjacent Zn and Sn atoms. According to the Pauling electronegativity scale, the N atom has a larger electronegativity (3.04) than the Sn (1.96) and Zn (1.65) atoms, which results in a large difference in electron density.

The cohesive energy per atom that quantifies the stability of materials is calculated using  $E_{\text{coh}} = [E_{\text{tot}} - (2E_{\text{Zn}} + 2E_{\text{Sn}} + 4E_{\text{N}})]/8$ , where  $E_{\text{Zn}}$ ,  $E_{\text{Sn}}$ , and  $E_{\text{N}}$  represent the energies of isolated single Zn, Sn, and N atoms, respectively.  $E_{\text{tot}}$  represents the total energy of the ZSN; 8 stands for the total number of atoms in the primitive unit cell. The calculated cohesive energy of the ZSN is −27.5 eV/atom. The band structure with the corresponding density of states (DOS) and projected DOS (PDOS) of the ZSN monolayer is shown in Figure 1c. Notice that the ZSN monolayer is a semiconductor with a direct band gap of 0.64 eV within the PBE functional. Since the ZSN monolayer is a semiconductor, the HSE06 functional has also been used to study the electronic band structures, as displayed in Figure 1c. It is clear that the HSE06-based results are consistent with the PBE/GGA ones for the direct semiconductor band gap of ZSN and the calculated band gap value is 1.71 eV, which agrees well with a previous report.<sup>46</sup>



**Figure 2.** Optimized atomic structures and electronic band structure of the ZSN monolayer with several kinds of vacancies including  $V^{\text{Zn}}$ ,  $V^{\text{Sn}}$ ,  $V^{\text{N}}$ ,  $V^{\text{Zn+N}}$ , and  $V^{\text{Sn+N}}$ . The zero of energy is set at the Fermi level.



**Figure 3.** (a) DOS/PDOS considering PBE, (b) DOS considering HSE06, and (c) difference in spin density of the ZSN monolayer with several kinds of vacancies including  $V^{\text{Zn}}$ ,  $V^{\text{Sn}}$ ,  $V^{\text{N}}$ ,  $V^{\text{Zn+N}}$ , and  $V^{\text{Sn+N}}$ . The blue and red colors indicate spin-up and spin-down density, respectively. The zero of energy is set at the Fermi level.

**Table 2. Structural and Electronic Parameters of the Defected ZSN Monolayer Including the Lattice Constants  $a$ ,  $b$ , Bond Lengths of Zn–N ( $d_{\text{Zn-N}}$ ) and Sn–N ( $d_{\text{Sn-N}}$ ) around the Vacancy Region, Formation Energy ( $E_f$ ), Work Function ( $\Phi$ ), Magnetic Moment ( $M$ ), and Electronic States (ES) Specified as Metal (M), Ferromagnetic Metal (FM), Dilute Magnetic Semiconductor (DM-SC), and Semiconductor (SC)<sup>a</sup>**

sys.	$a, b$ (Å)	$d_{\text{Zn-N}}$ (Å)	$d_{\text{Sn-N}}$ (Å)	$E_f$ (e)	$\Phi$ (eV)	$M$ (eV)	ES ( $\mu_B$ )	$E_g$
$V^{\text{Zn}}$	13.59, 11.78	1.84	2.07	-6.41	4.86	2.0	DM-SC	2.06 (1.61)
$V^{\text{Sn}}$	13.64, 11.82	1.90	2.00	-11.15	4.72	4.0	DM-SC	2.14 (1.65)
$V^{\text{N}}$	13.69, 11.86	1.84	2.07	-11.73	3.74	0.0	M	
$V^{\text{N+Zn}}$	13.23, 11.46	1.93	1.99	-16.11	4.53	1.0	DM-SC	2.07 (1.62)
$V^{\text{N+Sn}}$	13.69, 11.86	1.82	1.98	-20.12	4.40	1.0	DM-SC	2.18 (1.65)

<sup>a</sup>The band gap of HSE06 ( $E_g$ ) for the spin-up (spin-down) channel is shown outside (inside) parentheses.

We found that the valence band maximum (VBM) and the conduction band minimum (CBM) are located at the  $\Gamma$  point.

From the DOS and PDOS of the ZSN monolayer (see Figure 1c), it is clear that the VBM is mainly contributed by N- $p_z$  states,

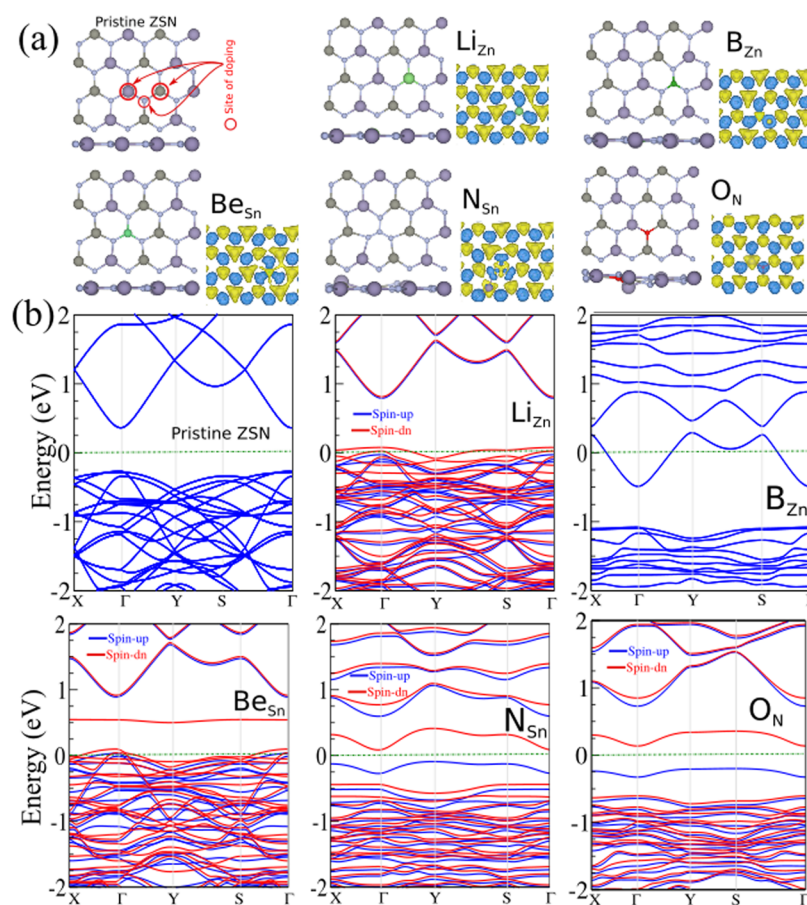


**Figure 4.** (a) Top and side views of the optimized structure and (b) electronic band structure of pristine ZSN with the site of doping, and doped ZSN with different atomic dopants such as  $\text{Li}_{\text{Zn}}$ ,  $\text{B}_{\text{Zn}}$ ,  $\text{Be}_{\text{Sn}}$ ,  $\text{N}_{\text{Sn}}$ , and  $\text{O}_{\text{N}}$ . Difference in charge density is indicated on the right side of the atomic structure. The zero of energy is set at the Fermi energy.

while the CBM is contributed by N- $p_{xy}$  and Zn-d states. To have an experimental insight, DFT is employed to simulate the STM image and the result is displayed in Figure 1d. Notice that the atomistic structure is easily recognized from the predicted STM image, where the N atoms are brighter than the Zn and Sn atoms.

First, we discuss the role of single and double vacancy defects in the structural and electronic properties of the ZSN monolayer. The vacancy defects include single vacancies Zn ( $\text{V}^{\text{Zn}}$ ), Sn ( $\text{V}^{\text{Sn}}$ ), and N ( $\text{V}^{\text{N}}$ ) as well as double vacancies N + Zn ( $\text{V}^{\text{N+Zn}}$ ) and N + Sn ( $\text{V}^{\text{N+Sn}}$ ).

The optimized atomic structures and electronic band structure of the ZSN monolayer for different vacancies are depicted in Figure 2a,b. Furthermore, the DOS/PDOS within the PBE of defected ZSN is shown in Figure 3a. For  $\text{V}^{\text{Zn}}$ , the bond lengths of N–Zn and N–Sn at the edge of a vacancy are determined to be 1.84 and 2.07 Å, respectively. The structural parameters including the bond lengths of defected ZSN with different point defects are listed in Table 2. The charge transfer calculations demonstrate that the N atom gains  $1.3e$  from the neighboring Zn and Sn atoms. We found that the work function value of  $\text{V}^{\text{Zn}}$  is 4.86 eV. From the band structure Figure 2b for  $\text{V}^{\text{Zn}}$ , one can see that the created midgap states for the N-p spin-up channel reduce the band gap from 0.64 to 0.4 eV. Meanwhile, due to the splitting bands of both spin components, the structure has a magnetic moment of  $2 \mu_{\text{B}}$ .

For  $\text{V}^{\text{Sn}}$ , with an optimized atomic structure shown in Figure 2a, the N–Zn and N–Sn bond lengths are 1.90 and 2 Å,

respectively. The related charge transfer values are the same as that for  $\text{V}^{\text{Sn}}$  and the work function is 4.72 eV. The created midgap states of N for the spin-up channel and Sn and Zn for the spin-down channel decrease the band gap to 0.3 eV. Meanwhile, for  $\text{V}^{\text{N}}$ , the bond lengths of N–Zn and N–Sn are determined to be 1.84 and 2.07 Å, respectively. The work function value of this defect is calculated as 3.74 eV. Figure 2b shows that  $\text{V}^{\text{N}}$  is p-type conducting with a band gap of 1 eV and there is spin degeneracy with nonmagnetic behavior. As regards the optimized atomic structures for double vacancies, the calculated bond lengths are 1.93 and 1.99 Å for the N–Zn and N–S, respectively (see Figure 2a). The work function value of  $\text{V}^{\text{N+Zn}}$  is determined to be 4.53 eV. Figure 2b shows the p-type conducting feature of the ZSN monolayer with a double vacancy  $\text{V}^{\text{N+Zn}}$ , having a band gap of 0.7 eV. The spin-up midgap states are dominated by the N-p orbital states with a small contribution of the Zn- and Sn-orbital states (see Figure 3a). The asymmetric DOS for the two spin components confirms the magnetic behavior of the structure with a magnetic moment of  $1 \mu_{\text{B}}$ . For the last type of vacancy considered in this study,  $\text{V}^{\text{N+Sn}}$  with an atomic structure illustrated in Figure 2a, the computed N–Zn and N–S bond lengths are 1.82 and 1.98 Å, respectively, and the work function value is 4.40 eV. The magnetic moment of  $\text{V}^{\text{N+Sn}}$  is similar to the corresponding value of  $\text{V}^{\text{N+Zn}}$ . From the band structure and DOS we found that the structure is metallic due to the dominant contributions of the N-p states in the two spin components at the Fermi energy (see Figure 3a).

**Table 3. Structural and Electronic Parameters of the Doped ZSN Monolayer Including the Lattice Constants  $a$ ,  $b$ , Bond Lengths of Zn–N ( $d_{\text{Zn-N}}$ ) and Sn–N ( $d_{\text{Sn-N}}$ ), Bond Lengths of the Dopant with a Nearest Host Atom ( $d_{\text{X}}$ ), the Charge Transfer ( $\Delta q$ ) Where the Positive (Negative) Denote to Lose (Gain) Charge, Formation Energy ( $E_{\text{ad}}$ ), Work Function ( $\Phi$ ), Magnetic Moment ( $M$ ), Electronic States (ES) Specified as Metal (M) and Dilute Magnetic Semiconductor (DM-SC), and Band Gap of HSE06 ( $E_{\text{g}}$ ) for the Spin-up (Spin-down) Channel is Shown Outside (Inside) Parentheses**

sys.	$a, b$ (Å)	$d_{\text{Zn-N}}$ (Å)	$d_{\text{Sn-N}}$ (Å)	$d_{\text{X}}$ (e)	$\Delta q$ (eV)	$E_{\text{ad}}$ (eV)	$\Phi$ ( $\mu_{\text{B}}$ )	$M$ (eV)	ES	$E_{\text{g}}$
Li <sub>Zn</sub>	13.64, 11.82	1.93	1.99	1.93	+0.84	−5.67	4.94	0.9	DM-SC	1.75 (1.50)
B <sub>Zn</sub>	13.36, 11.58	1.93	1.99	1.48	+0.84	−13.0	3.85	0.0	M	
Be <sub>Sn</sub>	13.46, 11.66	1.93	1.99	1.67	+1.60	−3.39	5.00	1.5	DM-SC	0.35 (1.70)
N <sub>Sn</sub>	12.92, 11.42	1.93	1.99	1.32	−1.00	−9.20	4.33	1.0	DM-SC	1.50 (1.25)
O <sub>N</sub>	13.61, 11.79	1.94	2.07	1.96	−1.10	−6.56	4.38	0.8	DM-SC	1.42 (1.40)

Since the defected ZSN monolayer shows a semiconducting character, the HSE06 functional has also been employed to study the material's electronic properties. The DOSs considering the HSE06 for the defected ZSN monolayer with several kinds of vacancies, including  $V^{\text{Zn}}$ ,  $V^{\text{Sn}}$ ,  $V^{\text{N}}$ ,  $V^{\text{Zn+N}}$ , and  $V^{\text{Sn+N}}$ , are illustrated in Figure 3b. Based on the band structure acquired by the HSE06 method,  $V^{\text{Zn}}$ ,  $V^{\text{Sn}}$ ,  $V^{\text{Zn+N}}$ , and  $V^{\text{Sn+N}}$  exhibit the behavior of a dilute magnetic semiconductor. For  $V^{\text{N}}$ , we observed a metallic behavior that is consistent with the PBE results. Our results demonstrate that the band gap in the spin-up (spin-down) channel for  $V^{\text{Zn}}$  and  $V^{\text{Sn}}$  is 2.06 eV (1.61) and 2.14 eV (1.65), respectively. Meanwhile, for the double vacancies  $V^{\text{N+Zn}}$  and  $V^{\text{N+Sn}}$ , the band gap values in the spin-up (spin-down) channel are estimated to be 2.07 eV (1.62) and 2.18 eV (1.65), respectively.

Figure 3c shows the difference in the spin density of the defected ZSN monolayer. It is clear that the majority of spin density comes from the N atoms that are located at the edge of the vacancy. The formation energy ( $E^{\text{f}}$ ), which gives an indication as to which Y vacancy is more likely to be of experimental relevance than the others, is defined as  $E^{\text{f}} = E^{\text{pristine}} - E^{\text{vacancy}} - E^{\text{Y}}$ , where  $E^{\text{vacancy}}$ ,  $E^{\text{Y}}$ , and  $E^{\text{pristine}}$  refer to the total energy of the ZSN monolayer with a Y vacancy, an isolated Y atom, and of a pristine structure, respectively. We determined  $E^{\text{Zn}}$  ( $E^{\text{Sn}}$ ) from the Zn (Sn) isolated atom energy, while we assume  $E^{\text{N}}$  to be half of the molecular energy. In our results, the formation energies of different single vacancies such as  $V^{\text{Zn}}$ ,  $V^{\text{Sn}}$ , and  $V^{\text{N}}$  were −6.41, −11.15, and −11.73 eV, respectively. Meanwhile, for the  $V^{\text{N+Zn}}$  and  $V^{\text{N+Sn}}$  double vacancy structures, the formation energies were calculated as −16.11 and −20.12 eV, correspondingly. Further, we examined the thermal stability of the ZSN monolayer with different vacancies of atoms by evaluating the ab initio molecular dynamics trajectories at 500 K. The AIMD simulation of the defected ZSN monolayer at 500 K is depicted in Figure S1 of the Supporting Information. The top and side views of the structures are indicated at the bottom panel of Figure S1. Analysis of the AIMD trajectories also shows the structure could stay intact at 500 K with very stable energy and temperature profiles, proving the thermal stability of the defected ZSN monolayer-based structures.

Most donor and acceptor impurities reside on substitutional sites, i.e., they replace one of the host atoms. Further, we investigated the effect of substitutional doping on the electronic properties of the ZSN monolayer. Figure 4a shows the top and side views of the relaxed structures of the pristine and doped ZSN monolayer, along with the calculated band structure and the pertinent charge transfer analysis. The Zn atom is replaced by Li (Li<sub>Zn</sub>) and B (B<sub>Zn</sub>). The Sn atom is substituted by Be (Be<sub>Sn</sub>) and N (N<sub>Sn</sub>). The structural parameters including the bond length of the ZSN monolayer with a different atomic

dopant are listed in Table 3. The last doped structure is the anionic dopant, where the N atom is replaced by an O atom (O<sub>N</sub>). We have determined that the optimized bond lengths are as follows: 1.93 (1.48 Å) for Li–N (B–N) in Li<sub>Zn</sub> (B<sub>Zn</sub>), 1.67 (1.32 Å) for Be–Sn (N–Sn) in Be<sub>Sn</sub>, and 1.96 (2.07 Å) for O–Zn (O–Sn) in the O<sub>N</sub> system. Obviously, as the atomic radius of the dopant increases, the bond length increases too. From Figure 4a, it is clear that the bond lengths and angles have a trivial effect on the planar structures, except in the case of substitution of N atom by an O atom. The charge transfer calculations imply that Zn, Sn, Li, B, and Be lose 1e, 1.6e, 0.84e, 2.1e, and 1.6e, respectively, while N and O (as dopants) gain 1e and 1.1e, respectively, from the surrounding atoms of the corresponding doped structures. These observations indicate a character of covalent bonding and chemisorption. The calculated work function values are 4.94, 3.85, 5.00, 4.33, and 4.38 eV for the Li<sub>Zn</sub>, B<sub>Zn</sub>, Be<sub>Sn</sub>, N<sub>Sn</sub>, and O<sub>N</sub> structures, correspondingly.

Obviously, as the atomic radius of the dopant increases, the bond length increases too. From Figure 4, it is clear that the bond lengths and angles have a trivial effect on the planar structures, except in the case of substitution of an N atom by an O atom. The charge transfer calculations imply that Zn, Sn, Li, B, and Be lose 1e, 1.6e, 0.84e, 2.1e, and 1.6e, respectively, while N and O (as dopants) gain 1e and 1.1e, respectively, from the surrounding atoms of the corresponding doped structures. These observations indicate a character of covalent bonding and chemisorption. The calculated work function values are 4.94, 3.85, 5.00, 4.33, and 4.38 eV for the Li<sub>Zn</sub>, B<sub>Zn</sub>, Be<sub>Sn</sub>, N<sub>Sn</sub>, and O<sub>N</sub> structures, correspondingly.

To explain the origin of the electronic states, the DOS and PDOS of the doped ZSN monolayer within PBE are shown in Figures 4b and 5, respectively. For Li<sub>Zn</sub>, as compared to the pristine ZSN, we can see that the Fermi energy is shifted toward the lower energies due to the effect of the Li dopant. The structure is p-type conducting with the same band gap value as the pristine ZSN monolayer. Notice that the break in the electronic degeneracy in the up and down spin channels induces a magnetic moment of 0.8  $\mu_{\text{B}}$  in the ground state. The N-p and Sn-p states are dominant in the VB and CB, respectively. The contribution of the Li states appears in the VB (from −2.5 to 0.1 eV) and in the shown range of the CB. As regards B<sub>Zn</sub>, the Fermi energy is shifted toward the CB, which means that the structure is n-type conducting and nonmagnetic. The band gap becomes 0.6 eV, which is smaller than the corresponding value of the pristine ZSN and Li<sub>Zn</sub> structures (see Figure 4b). The dominant states at the top of the VB and the bottom of the CB are similar to those of Li<sub>Zn</sub>. The contribution of the B states is larger than the contribution of the Li states. Turning to the substitutional dopants residing on the Sn atom site, the band structure and PDOS of Be<sub>Sn</sub> are demonstrated in Figures 4b and 5. Notably,

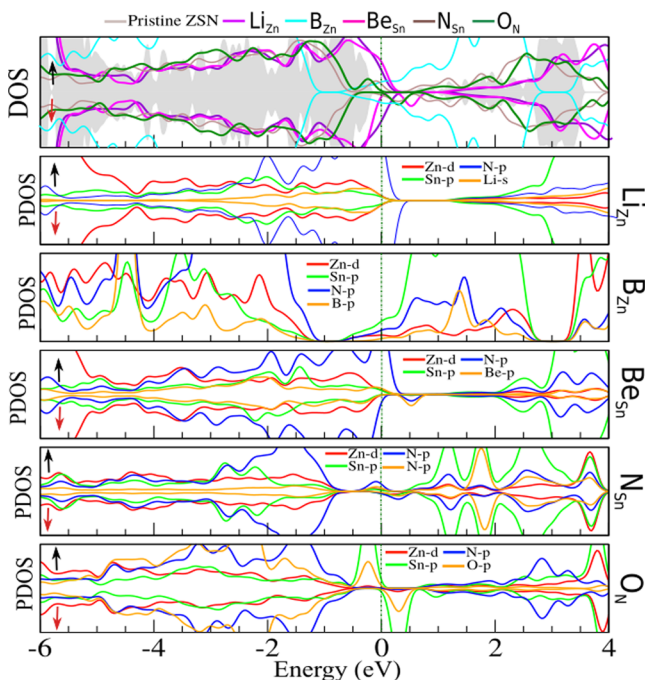


**Figure 5.** DOS of doped ZSN with different atomic dopants such as  $\text{Li}_{\text{Zn}}$ ,  $\text{B}_{\text{Zn}}$ ,  $\text{Be}_{\text{Sn}}$ ,  $\text{N}_{\text{Sn}}$ , and  $\text{O}_{\text{N}}$ . The zero of energy is set at the Fermi energy.

the Fermi energy is shifted toward the lower energies, which means that the structure is p-type conducting. The asymmetry in the band structure/PDOS induces a magnetic moment of  $1.5 \mu_{\text{B}}$ . The contribution of Be states at the top of the VB decreases the band gap value to 0.5 eV. In the case of  $\text{N}_{\text{Sn}}$ , we can see band splitting in both the spin-up and spin-down channels, as compared to the pristine ZSN, and the system turns out to be a

magnetic semiconductor. The asymmetry in the two spin components of the band structure/PDOS refers to a magnetic structure with a magnetic moment of  $1 \mu_{\text{B}}$ . The anionic dopant is the last dopant considered in this study, namely, the oxygen atom on a nitrogen site,  $\text{O}_{\text{N}}$ , which is largely observed in 3D-ZSN. Figure 5 demonstrates that the O and Sn states are filling the band gap, as compared to the pristine ZSN monolayer, and  $\text{O}_{\text{N}}$  is a semiconductor with a magnetic moment of  $0.88 \mu_{\text{B}}$  due to the asymmetry in both spin components of the  $\text{O}_{\text{N}}$  density of states.

Since the doped ZSN monolayer shows a semiconducting character, the HSE06 functional was also used to study the electronic properties. The DOS considering HSE06 for the doped ZSN monolayer with several kinds of atomic dopants including  $\text{Li}_{\text{Zn}}$ ,  $\text{B}_{\text{Zn}}$ ,  $\text{Be}_{\text{Sn}}$ ,  $\text{N}_{\text{Sn}}$ , and  $\text{O}_{\text{N}}$  is shown in Figure S1 of the Supporting Information (SI). Based on the acquired band structure by the HSE06 method,  $\text{Li}_{\text{Zn}}$ ,  $\text{B}_{\text{Zn}}$ ,  $\text{Be}_{\text{Sn}}$ ,  $\text{N}_{\text{Sn}}$ , and  $\text{O}_{\text{N}}$  are dilute magnetic semiconductors. We found that the band gaps in the spin-up (spin-down) channel for  $\text{Li}_{\text{Zn}}$  and  $\text{B}_{\text{Zn}}$  were 1.75 eV (1.50) and 1.35 eV (1.53), respectively. However, for  $\text{N}_{\text{Sn}}$  and  $\text{O}_{\text{N}}$ , the band gaps in the spin-up (spin-down) channel were 1.50 eV (1.25) and 1.42 eV (1.40), respectively.

Further, we examined the thermal stability of the ZSN monolayer doped with different dopants by evaluating the ab initio molecular dynamics trajectories at 500 K. The ab initio molecular dynamics simulation of the doped ZSN monolayer at 500 K and at room temperature is exhibited in Figure 6. The top and side views of the structures are depicted at the top panel. The analysis of the AIMD trajectories shows that the structures could stay intact at 500 K, with very stable energy and temperature profiles, indicating the thermal stability of the doped ZSN structures.

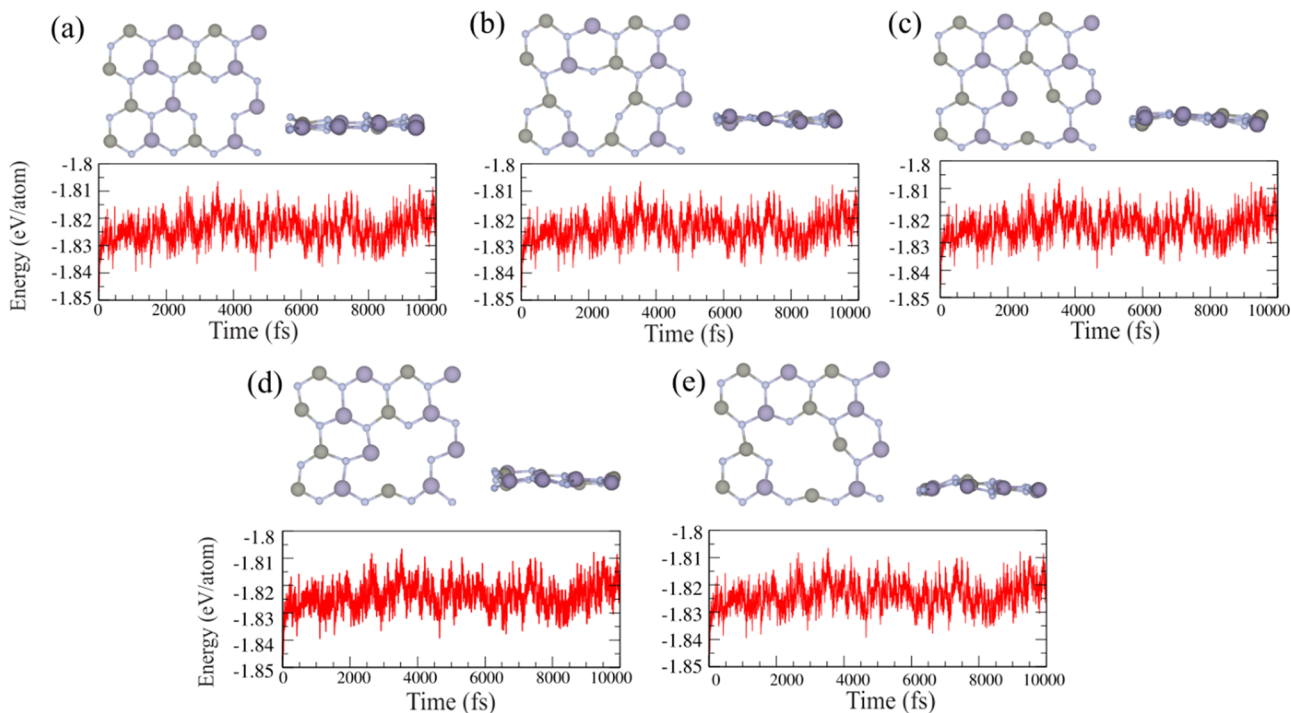


**Figure 6.** Ab initio molecular dynamics at 500 K (top) and top and side views of atomic structures after AIMD simulation (bottom) for the (a)  $\text{V}_{\text{Zn}}^{\text{Zn}}$ , (b)  $\text{V}_{\text{Sn}}^{\text{Sn}}$ , (c)  $\text{V}_{\text{N}}^{\text{N}}$ , (d)  $\text{V}_{\text{Zn}}^{\text{Sn}}$ , and (e)  $\text{V}_{\text{Sn}}^{\text{N}}$  ZSN defected monolayer.

## CONCLUSIONS

The electronic and magnetic properties of a pristine and a defected ZnSnN<sub>2</sub> monolayer have been studied by the spin density functional theory. Different kinds of vacancy defects have been considered, such as Zn, Sn, N, N + Zn, and N + Sn vacancies. Moreover, several substitutional dopants situated at different host atom positions have been investigated: Li and B (at the Zn site), Be and N (at the Sn site), and O (at the N site). We found that the Zn and Sn vacancy structures have higher work function values as compared to the pristine ZSN monolayer and the other vacancy structures. All ZSN monolayer-based structures containing vacancies possess magnetic properties except the one with the nitrogen vacancy. The vacancy-defected structures are of p-type for Zn, Sn, N, and N + Zn vacancies, of n-type for the N vacancy, and with a metallic behavior for the N + Sn vacancy. The results of the ab initio molecular dynamics simulation confirm that all substitutionally doped and defected structures are thermally stable. We found that Be<sub>Sn</sub> has the largest work function value within this study (5.0 eV). Li<sub>Zn</sub> and Be<sub>Sn</sub> are p-type, while B<sub>Zn</sub> is n-type, and all doped ZSN monolayers have magnetic properties except B<sub>Zn</sub>.

## ASSOCIATED CONTENT

### Supporting Information

The Supporting Information is available free of charge at <https://pubs.acs.org/doi/10.1021/acs.jpcc.1c03749>.

DOS considering HSE06 for doped ZSN monolayers with different atomic dopants (PDF)

## AUTHOR INFORMATION

### Corresponding Authors

**Asadollah Bafekry** – Department of Radiation Application, Shahid Beheshti University, 1983969411 Tehran, Iran; Department of Physics, University of Antwerp, B-2020 Antwerp, Belgium; [orcid.org/0000-0002-9297-7382](https://orcid.org/0000-0002-9297-7382); Email: [bafekry.asad@gmail.com](mailto:bafekry.asad@gmail.com)

**Mitra Ghergherehchi** – Department of Electrical and Computer Engineering, Sungkyunkwan University, 16419 Suwon, Korea; Email: [mitragh@skku.edu](mailto:mitragh@skku.edu)

### Authors

**Mehrdad Faraji** – Micro and Nanotechnology Graduate Program, TOBB University of Economics and Technology, 06560 Ankara, Turkey

**Mohamed M. Fadlallah** – Department of Physics, Faculty of Science, Benha University, 13518 Benha, Egypt

**Bohayra Mortazavi** – Chair of Computational Science and Simulation Technology, Institute of Photonics, Department of Mathematics and Physics, Leibniz University Hannover, 30167 Hannover, Germany; [orcid.org/0000-0003-3031-5057](https://orcid.org/0000-0003-3031-5057)

**A. Abdolhazadeh Ziabari** – Nano Research Lab, Lahijan Branch, Islamic Azad University, 1616 Lahijan, Iran

**A. Bagheri Khatibani** – Nano Research Lab, Lahijan Branch, Islamic Azad University, 1616 Lahijan, Iran

**Chuong V. Nguyen** – Department of Materials Science and Engineering, Le Quy Don Technical University, Hanoi 100000, Vietnam; [orcid.org/0000-0003-4109-7630](https://orcid.org/0000-0003-4109-7630)

**Daniela Gogova** – Department of Physics, University of Oslo, Oslo, Norway

Complete contact information is available at: <https://pubs.acs.org/doi/10.1021/acs.jpcc.1c03749>

## Notes

The authors declare no competing financial interest.

## ACKNOWLEDGMENTS

This work was supported by the National Research Foundation of Korea Grant funded by the Korean government (MSIT) (NRF-2015M2B2A4033123). B.M. appreciates the funding by the Deutsche Forschungsgemeinschaft (DFG, German Research Foundation) under Germany's Excellence Strategy within the Cluster of Excellence PhoenixD (EXC 2122, Project ID 390833453).

## REFERENCES

- (1) Haseman, M. S.; Karim, M. R.; Ramdin, D.; Noesges, B. A.; Feinberg, E.; Jayatunga, B.; Lambrecht, W.; Zhu, M.; Hwang, J.; Kash, K.; et al. Deep level defects and cation sublattice disorder in ZnGeN<sub>2</sub>. *J. Appl. Phys.* **2020**, *127*, No. 135703.
- (2) Gogova, D.; Olsen, V. S.; Baziotti, C.; Lee, I. H.; Prytz, O.; Vines, L.; Kuznetsov, A. Y. High electron mobility single-crystalline ZnSnN<sub>2</sub> on ZnO (0001) substrates. *CrystEngComm* **2020**, *22*, 6268.
- (3) Skachkov, D.; Jaroenjittichai, A. P.; Huang, L.; Lambrecht, W. R. L. Native point defects and doping in ZnGeN<sub>2</sub>. *Phys. Rev. B* **2016**, *93*, No. 155202.
- (4) Khan, I. S.; Heinselman, K.; Zakutayev, A. Review of ZnSnN<sub>2</sub> semiconductor material. *J. Phys. Energy* **2007**, *3*, No. 032007.
- (5) Wang, T.; Ni, C.; Janotti, A. Band alignment and p-type doping of ZnSnN<sub>2</sub>. *Phys. Rev. B* **2017**, *95*, No. 205205.
- (6) Veal, T. D.; Feldberg, N.; Quackenbush, N. F.; Linhart, W. M.; Scanlon, D. O.; Piper, L. F. J.; Durbin, S. M. Band Gap Dependence on Cation Disorder in ZnSnN<sub>2</sub> Solar Absorber. *Adv. Energy Mater.* **2015**, *5*, No. 1501462.
- (7) Ye, F.; Chen, Q. Q.; Cai, X. M.; Xie, Y. Z.; Ma, X. F.; Vaithinathan, K.; Zhang, D. P.; Fan, P.; Roy, V. A. L. Improving the chemical potential of nitrogen to tune the electron density and mobility of ZnSnN<sub>2</sub>. *J. Mater. Chem. C* **2020**, *8*, 4314–4320.
- (8) Fang, D. Q.; Chen, X.; Gao, P. F.; Zhang, Y.; Zhang, S. L. Mono- and Bilayer ZnSnN<sub>2</sub> Sheets for Visible-Light Photocatalysis: First-Principles Predictions. *J. Phys. Chem. C* **2017**, *121*, 26063–26068.
- (9) Adamski, N. L.; Wickramaratne, D.; Van de Walle, C. G. Band alignments and polarization properties of the Zn-IV-nitrides. *J. Mater. Chem. C* **2020**, *8*, 7890–7898.
- (10) Cao, X.; Kawamura, F.; Taniguchi, T.; Yamada, N. Electron-transport properties of degenerate ZnSnN<sub>2</sub> doped with oxygen. *BMC Mater.* **2020**, *2*, No. 4.
- (11) Quayle, P. C.; He, K.; Shan, J.; Kash, K. Synthesis, lattice structure, and band gap of ZnSnN<sub>2</sub>. *MRS Commun.* **2013**, *3*, 135–138.
- (12) Feldberg, N.; Aldous, J. D.; Linhart, W. M.; Phillips, L. J.; Durose, K.; Stampe, P. A.; Kennedy, R. J.; Scanlon, D. O.; Vardar, G.; Field, R. L.; et al. Growth, disorder, and physical properties of ZnSnN<sub>2</sub>. *Appl. Phys. Lett.* **2013**, *103*, No. 042109.
- (13) Fioretti, A. N.; Zakutayev, A.; Moutinho, H.; Melamed, C.; Perkins, J. D.; Norman, A. G.; Al-Jassim, M.; Toberer, E. S.; Tamboli, A. C. Combinatorial insights into doping control and transport properties of zinc tin nitride. *J. Mater. Chem. C* **2015**, *3*, 11017–11028.
- (14) Paudel, T. R.; Lambrecht, W. R. L. First-principles study of phonons and related ground-state properties and spectra in Zn-IV-N<sub>2</sub> compounds. *Phys. Rev. B* **2008**, *78*, No. 115204.
- (15) Feldberg, N.; Keen, B.; Aldous, J. D.; Scanlon, D. O.; Stampe, P. A.; Kennedy, R. J.; Reeves, R. J.; Veal, T. D.; Durbin, S. M. In *ZnSnN<sub>2</sub>: A New Earth-Abundant Element Semiconductor for Solar Cells*, IEEE: New York, 2012; pp 2524–2527.
- (16) Coronel, N. C.; Lahourcade, L.; Delaney, K. T.; Shing, A. M.; Atwater, H. A. In *Earth-Abundant ZnSn<sub>x</sub>Ge<sub>1-x</sub>N<sub>2</sub> Alloys as Potential Photovoltaic Absorber Materials*, Proceedings of the 38th IEEE Photovoltaic Specialists Conference; IEEE: New York, 2012; pp 3204–3207.

- (17) Kawamura, F.; Yamada, N.; Imai, M.; Taniguchi, T. Synthesis of ZnSnN<sub>2</sub> crystals via a high pressure metathesis reaction. *Cryst. Res. Technol.* **2016**, *51*, 220–224.
- (18) Cao, X.; Kawamura, F.; Ninomiya, Y.; Taniguchi, T.; Yamada, N. Conduction-band effective mass and bandgap of ZnSnN<sub>2</sub> earth abundant solar absorber. *Sci. Rep.* **2017**, *7*, No. 14987.
- (19) Chinnakutti, K. K.; Vengatesh, P.; Shyju, T. S. Tailoring optoelectronic properties of earth abundant ZnSnN<sub>2</sub> by combinatorial RF magnetron sputtering. *J. Alloys Compd.* **2019**, *772*, 348–358.
- (20) Tsunoda, N.; Kumagai, Y.; Takahashi, A.; Oba, F. Electrically Benign Defect Behavior in Zinc Tin Nitride Revealed from First Principles. *Phys. Rev. Appl.* **2018**, *10*, No. 011001.
- (21) Punya, A.; Paudel, T. R.; Lambrecht, W. R. L. Electronic and lattice dynamical properties of II-IV-N<sub>2</sub> semiconductors. *Phys. Status Solidi C* **2011**, *8*, 2492–2499.
- (22) Punya, A.; Lambrecht, W. R. L.; Van Schilfgaarde, M. Quasiparticle band structure of Zn-IV-N<sub>2</sub> compounds. *Phys. Rev. B* **2011**, *84*, No. 165204.
- (23) Narang, P.; Chen, S.; Coronel, N. C.; Gul, S.; Yano, J.; Wang, L. W.; Lewis, N. S.; Atwater, H. A. Bandgap tunability in Zn(Sn,Ge)N<sub>2</sub> semiconductor alloys. *Adv. Mater.* **2014**, *26*, 1235.
- (24) Lahourcade, L.; Coronel, N. C.; Delaney, K. T.; Shukla, S. K.; Spaldin, N. A.; Atwater, H. A. Structural and Optoelectronic Characterization of RF Sputtered ZnSnN<sub>2</sub>. *Adv. Mater.* **2013**, *25*, 2562.
- (25) Punya, A.; Lambrecht, W. R. L. Band offsets between ZnGeN<sub>2</sub>, GaN, ZnO, and ZnSnN<sub>2</sub> and their potential impact for solar cells. *Phys. Rev. B* **2013**, *88*, No. 075302.
- (26) Quayle, P. C.; Blanton, E. W.; Punya, A.; Junno, G. T.; He, K.; Han, L.; Zhao, H.; Shan, J.; Lambrecht, W. R. L.; Kash, K. Charge-neutral disorder and polytypes in heterovalent wurtzite-based ternary semiconductors: The importance of the octet rule. *Phys. Rev. B* **2015**, *91*, No. 205207.
- (27) Deng, F.; Cao, H.; Liang, L.; Li, J.; Gao, J.; Zhang, H. Determination of the basic optical parameters of ZnSnN<sub>2</sub>. *Opt. Lett.* **2015**, *40*, 1282–1285.
- (28) Chen, S.; Narang, P.; Atwater, H. A.; Wang, L. W. Phase Stability and Defect Physics of a Ternary ZnSnN<sub>2</sub> Semiconductor: First Principles Insights. *Adv. Mater.* **2014**, *26*, 311–315.
- (29) Wu, X. J.; Meng, F. Z.; Chu, D. L.; Yao, M. C.; Guan, K.; Zhang, D. D.; Meng, J. Carrier Tuning in ZnSnN<sub>2</sub> by Forming Amorphous and Microcrystalline Phases. *Inorg. Chem.* **2019**, *58*, 8480–8485.
- (30) Alnjiman, F.; Diliberto, S.; Ghanbaja, J.; Haye, E.; Kassavetis, S.; Patsalas, P.; Gendarme, C.; Bruyere, S.; Cleymand, F.; Boulet, P.; et al. Chemical environment and functional properties of highly crystalline ZnSnN<sub>2</sub> thin films deposited by reactive sputtering at room temperature. *Sol. Energy Mater. Sol. Cells* **2018**, *182*, 30–36.
- (31) Skachkov, D.; Lambrecht, W. R. L. Candidates for p-type doping of ZnGeN<sub>2</sub>. *J. Appl. Phys.* **2020**, *127*, No. 075707.
- (32) Bhimanapati, G. R.; Lin, Z.; Meunier, V.; Jung, Y. G.; Cha, J.; Das, S.; Xiao, D.; Son, Y.; Strano, M. S.; Cooper, V. R.; et al. Recent Advances in Two-Dimensional Materials beyond Graphene. *ACS Nano* **2015**, *9*, 11509–11539.
- (33) Wang, S.; Robertson, A.; Warner, J. H. Atomic structure of defects and dopants in 2D layered transition metal dichalcogenides. *Chem. Soc. Rev.* **2018**, *47*, 6764–6794.
- (34) Rhodes, D.; Chae, S. H.; Ribeiro-Palau, R.; Hone, J. Disorder in van der Waals heterostructures of 2D materials. *Nat. Mater.* **2019**, *18*, 541–549.
- (35) Perdew, J. P.; Burke, K.; Ernzerhof, M. Generalized gradient approximation made simple. *Phys. Rev. Lett.* **1996**, *77*, 3865.
- (36) Perdew, J. P.; Burke, K.; Ernzerhof, M. Generalized gradient approximation made simple. *Phys. Rev. Lett.* **1997**, *78*, No. 1396.
- (37) Kresse, G.; Hafner, J. Ab initio molecular dynamics for liquid metals. *Phys. Rev. B* **1993**, *47*, No. 558.
- (38) Kresse, G.; Hafner, J. Efficient iterative schemes for ab initio total-energy calculations using a plane-wave basis set. *Phys. Rev. B* **1994**, *49*, No. 14251.
- (39) Heyd, J.; Scuseria, G. E.; Ernzerhof, M. Screened hybrid density functionals applied to solids. *J. Chem. Phys.* **2003**, *118*, 8207.
- (40) Monkhorst, H. J.; Pack, J. D. Special points for Brillouin-zone integrations. *Phys. Rev. B* **1976**, *13*, No. 5188.
- (41) Henkelman, G.; Arnaldsson, A.; Jonsson, H. A fast and robust algorithm for Bader decomposition of charge density. *Comput. Mater. Sci.* **2006**, *36*, 354.
- (42) Grimme, S. J. Semiempirical GGA-type density functional constructed with a long-range dispersion correction. *J. Comput. Chem.* **2006**, *27*, 1787.
- (43) Alfè, D. PHON: A program to calculate phonons using the small displacement method. *Comput. Phys. Commun.* **2009**, *180*, 2622.
- (44) Tersoff, J.; Hamann, D. R. Theory and Application for the Scanning Tunneling Microscope. *Phys. Rev. Lett.* **1983**, *50*, 1998–2001.
- (45) Horcas, I.; Fernandez, R.; Gomez-Rodriguez, J. M.; Colchero, J.; Gomez-Herrero, J.; Baro, A. M. WSXM: A software for scanning probe microscopy and a tool for nanotechnology. *Rev. Sci. Instrum.* **2007**, *78*, No. 013705.
- (46) Bai, Y.; Luo, G.; Meng, L.; Zhang, Q.; Xu, N.; Zhang, H.; Wu, X.; Kong, F.; Wang, B. Single-layer ZnMN<sub>2</sub> (M = Si, Ge, Sn) zinc nitrides as promising photocatalysts. *Phys. Chem. Chem. Phys.* **2018**, *20*, 14619.